Ocean mixing in a shelf sea driven by energetic internal waves

C. A. Whitwell[1], N. L. Jones[1], G. N. Ivey[1], M. G. Rosevear[1,2], and M. D. Rayson[1]

[1]Oceans Graduate School and Oceans Institute, University of Western Australia, Crawley, Western Australia, Australia
[2]Department of Mechanical Engineering, University of Melbourne Australia, Parkville, Victoria, Australia

Key Points:

- A few energetic short-lived nonlinear internal wave events drove most of the vertical turbulent heat flux over the month-long record.
- Internal wave events evolved over relatively short space and time scales.
- Energetic internal wave events contribute significantly to mixing in shelf seas.

Corresponding author: Chris Whitwell, chris.a.whitwell@outlook.com

Abstract

We collected observations of ocean mixing from three moorings placed at the 330m, 200m, and 150m isobaths on a pelagic ridge on the Australian North West Shelf (NWS). The region is subject to energetic surface and internal tides, non-linear internal waves, flow-topography interactions, and episodic intense wind events (i.e., tropical cyclones) that collectively drive energetic diapycnal mixing. We identified five dominant internal wave categories: both low (time scales from double the buoyancy period to 4 hours) and high-frequency (time scales between buoyancy period and double the buoyancy period) mode-1 waves, mode-2 waves, internal bores, and internal hydraulic jumps. A small number of turbulent mixing events dominated the total vertical heat flux at each mooring, with 15% of estimates accounting for as much as 90% of the total observed heat flux. These turbulent mixing events often occurred during the passage of internal wave events, with the internal wave events accounting for as much as 60% of the total heat flux in some locations. High-frequency mode-1 waves were the most significant contributors to the total vertical heat flux ($\sim$ 20%). Internal bores made significant but localized contributions to mixing, accounting for up to $\sim$ 50% of the total vertical heat flux in some regions but with a negligible influence elsewhere. The contributions of the different internal wave categories to the total flux became more heterogeneous at shallower sites, indicating an increasingly complicated relationship between the forcing internal wave field and the mixing.

Plain Language Summary

Internal waves propagate along the density gradients found beneath the ocean's surface layer, analogous to surface waves propagating along the sharp density gradient where air and water meet. These waves play an important role in the distribution of nutrients, heat, contaminants, and other tracers in the ocean, especially in coastal regions where they break. The density structure of the ocean, the tidal and wind forcing, and the seabed features result in many different types of internal waves, each of which travel and break differently. In this work, we examine the mixing caused by different types of internal waves as they travel up a subsurface ridge on the Australian North West Shelf. We found that most of the significant mixing resulted from relatively rare events, which often occurred due to internal wave activity. The magnitude of mixing increased in shallower waters due to internal waves breaking and causing energetic turbulent flows. However, the most important types of waves for mixing changed greatly depending on the location. High-frequency internal waves were generally the most significant contributor to mixing. However, internal bores, a class of waves moving upslope near the seabed, dominated the total ocean mixing at some locations.

1 Introduction

Diapycnal mixing describes the transport of heat, salt, momentum and passive tracers in the ocean's stratified regions. In shelf seas, diapycnal mixing is important for transporting nutrient-rich water into the well-lit surface layer (Huisman et al., 2006), mitigating thermal stress events (Wyatt et al., 2020) and the distribution of other tracers such as contaminants. Efforts to compile field estimates of mixing provide a picture of the spatial variability of mixing (Inall et al., 2021; Waterhouse et al., 2014). However, how representative these estimates are is unclear, given the vast scale of the ocean and the inherent spatial and temporal variability of mixing. As a result, the dynamics that control mixing are still not well understood, leading to uncertainty in parameterizing mixing in ocean models (e.g. Savelyev et al., 2022), where mixing processes are inadequately resolved. The challenge of resolving mixing in ocean models is further amplified by the fact that processes responsible for generating mixing, such as internal waves (Whalen et al., 2020), are also poorly represented.

Internal waves are particularly important for driving diapycnal mixing in shelf seas where internal waves break and generate highly turbulent flows (Lamb, 2014). Internal waves are generated by tide-topography interactions (internal tides) both locally and remotely (Gong et al., 2021), via interactions with ridges (e.g. lee waves, see Legg, 2020), or by variable winds pumping the surface mixed layer (near-inertial waves) (Alford et al., 2016). Internal wave energy generated on the continental shelf can propagate towards both shallower and deeper water, and can dissipate energy via transfer to high wavenumbers and wave breaking (Lamb, 2014). The dissipation of internal wave energy and the consequent mixing on continental shelves is complex. Generally, internal wave-driven mixing occurs via shear instability, (local) convective instability, or both (Ivey et al., 2021). However, the location and timing of these instabilities are highly dependent on the local properties of both the internal wave itself, the background barotropic flow and the local density stratification. The cross-shelf evolution of the internal wave field further complicates these dynamics as internal wave energy is transferred between different wave types during shoaling and breaking (e.g. Aghsaee et al., 2010).

Most propagating internal wave energy is in low modes (1 and 2), with high modes dissipating quickly. Mode-1 waves, characterized by their in-phase isotherm displacements, are categorized as waves of elevation or depression depending on the sign of the isopycnal displacement. Mode-2 waves are characterized by diverging (convex) or converging (concave) isotherms. Internal wave energy is transferred between different waveforms during shoaling and breaking on the continental shelf. For example, convex mode-2 waves shoaling on continental slopes may develop a "tail" of mode-1 waves propagating in its wake before ultimately degenerating into mode-1 waves of elevation (Shroyer et al., 2010a; Carr et al., 2019). Internal bores (boluses), waves propagating along the bed characterized by sharp changes in density, may form due to the internal tide interacting with the slope or internal wave breaking (Winters, 2015; Ghassemi et al., 2022). Internal hydraulic jumps occur on the flanks of ridges in oscillatory flows, locally dissipating internal wave energy (Nash & Moum, 2001).

Observations indicate that mode-1 waves of depression can enhance mixing in the thermocline on the rear face of the waves and in the wave troughs where the shear is high (Shroyer et al., 2010b; MacKinnon & Gregg, 2003). Waves of elevation exhibit multiple breaking mechanisms with unique mixing fields that consist of shear and convective instabilities on either the front or rear face of the wave (N. L. Jones et al., 2020). Observations during mode-2 wave shoaling indicate that turbulent dissipation is enhanced at the wave peak where shear is enhanced, on the rear face of the wave and in the trailing mode-1 wavetrain (Shroyer et al., 2010a). Internal bores may enhance mixing on their leading edge via convective overturning or through both shear and convective instabilities on their trailing edge (N. L. Jones et al., 2020; Davis et al., 2020; Walter et al., 2012). Internal hydraulic flows and jumps can greatly enhance both shear- and convectively-driven mixing (Nash & Moum, 2001).

Despite these significant observational, numerical and laboratory investigations into the fate of internal waves and their associated mixing, the characterization of internal wave-driven mixing on continental shelves and slopes remains incomplete. Many investigations do not capture the diversity of internal wave forcing and spatiotemporal scales controlling mixing on continental shelves. Our study addresses gaps in internal wave-driven mixing on continental shelves by addressing the following questions:

1. Is the net mixing primarily driven by the typical forcing or by short-term intense "events"?
2. How do the dominant internal wave-driven mixing processes change over depth and across the shelf?
3. What types of internal waves dominate mixing in shelf seas?

Our study addresses these questions by utilizing recent field observations of mixing from a site forced by an energetic and highly variable tidally-driven internal wave field. We begin by describing the field experiment (Sections 2.1-2.2) and outline the techniques used to characterize the internal wave field (Section 2.3). We then describe two independent methods used to estimate ocean mixing (Section 2.4). We characterize the site dynamics and describe the observed internal wave events (Section 3.1) before providing an overview of the mixing model performance and corresponding mixing estimates (Section 3.2). By using four examples, we then illustrate internal wave driven mixing for the different wave types (Section 3.3). Finally, we show the cross-shelf evolution of the mechanisms driving ocean mixing (Section 3.4), and discuss the implications of these findings for the parameterization of mixing in coastal seas (Section 4).

2 Site Description and Methods

2.1 Site Description

The Australian North West Shelf (NWS) has strong and persistent density stratification with strong tidal forcing leading to the generation, shoaling and breaking of mode-1, mode-2 and higher order nonlinear internal waves (NLIW) (Gong et al., 2019; N. L. Jones et al., 2020). The region is also subject to tropical cyclones (TC) during the austral summer months. The Rowley Shoals 2019 experiment was conducted from 8th March to 5th April 2019 at a study site approximately 300km west of Broome, spanning a continental shelf ridge located southeast of Imperieuse Reef, the southernmost reef of the Rowley Shoals. Our field observations form a transect across the pelagic ridge (H. A. Jones, 1970) at a bearing of 135° from true north (Fig 1). The ridge slope varies (Fig 1b) along the transect from 0.5% at the north-westerly extent to 0.8% towards the ridge apex.

2.2 Mooring Configuration and Instrumentation

The deployment consisted of three moorings in a line at the 150m, 200m and 330m isobaths, respectively. The distance between the moorings at the 330m and 200m isobaths was ∼29km, and the distance between the 200m and 150m isobaths was ∼5.5km. Each of the moorings consisted of a bottom-mounted upward-facing acoustic-Doppler current profiler (ADCP), a string of thermistors at variable spacing, and a single conductivity-temperature sensor. The ADCPs at the T150 and T200/T330 moorings were 150kHz and 75kHz, respectively, and sampled the entire depth with 60s averages and 2m bins.

The 150m mooring was equipped with thermistors sampling at 1Hz at 2m, 5m and 10m spacing over the ranges 0-25m, 25-60m and 60-120m above the seabed (ASB), respectively. The 200m mooring was equipped with thermistors sampling at 1Hz with 5m and 10m spacing over the ranges 10-30m and 30-80m ASB, respectively, and thermistors sampling at 0.05Hz with 10m spacing over the range 80-170m ASB. The T330 mooring was equipped with thermistors sampling at 0.05Hz at 10m spacing for the entire depth.

The 200m mooring was equipped with a moored turbulence package (MTP) at 10m ASB. The MTP consisted of a Nortek Vector acoustic-Doppler velocimeter (ADV) equipped with a Microstrain inertial measurement unit (IMU). The ADV was collocated with a Rockland microSquid equipped with an FP-07 fast response thermistor, and the MTP sampled all channels at a nominal rate of 16Hz.

2.3 Characterizing the Internal Wave Field

We used the Korteweg-de Vries (KdV) equation, a weakly non-linear model, to estimate the theoretical internal wave response from the background stratification conditions at each mooring during the study. We then characterized the internal wave field

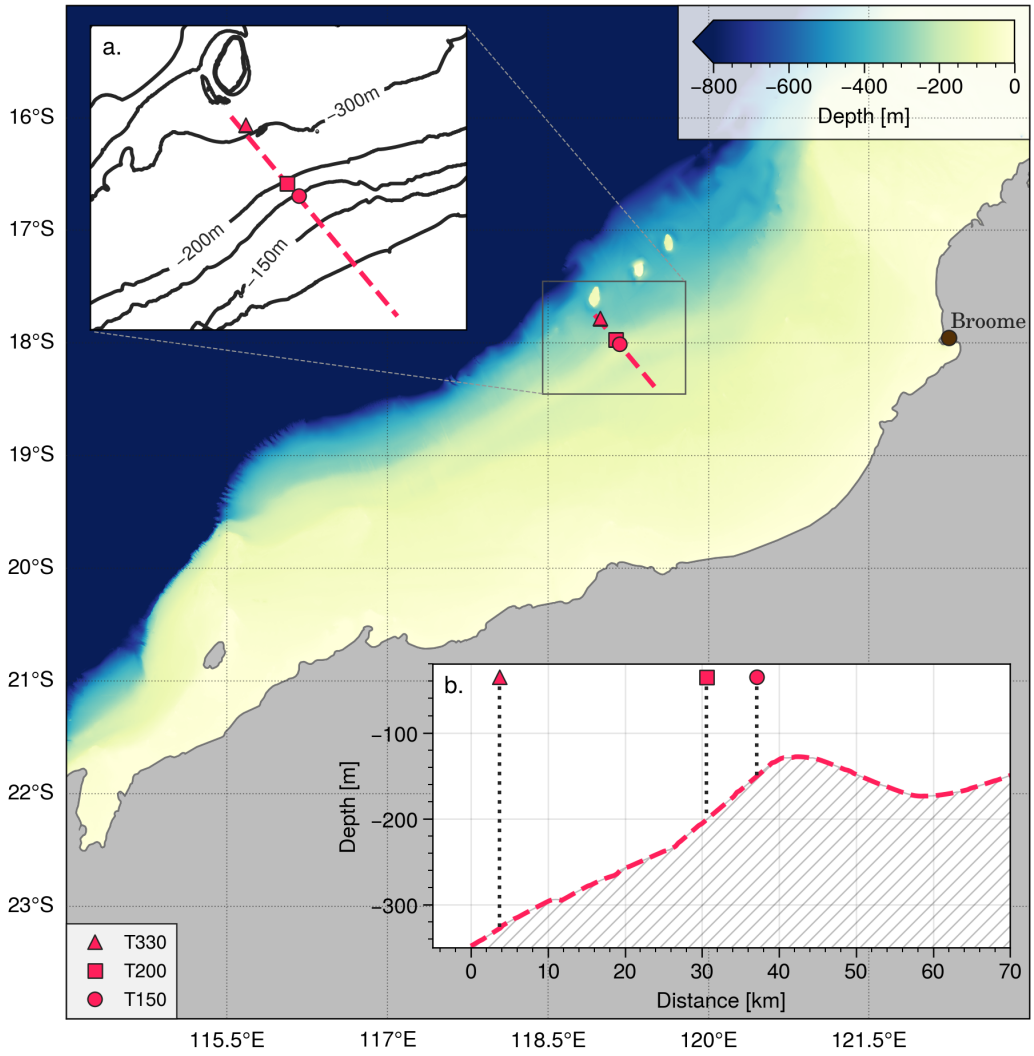

Figure 1. Map of the NWS showing the location of the Rowley Shoals 2019 mooring deployment. Inset (a) shows moorings (markers) and the local 50m depth contours. Inset (b) shows the depth along a cross-section of the moorings corresponding to the red dashed line in (a).

by using both modal amplitude fitting and tracking the near-bed temperature anomaly, and we used this information to identify internal wave events as described below.

2.3.1 Environmental Parameters

We followed Rayson et al. (2019) and used the KdV equation to characterize the internal wave environmental parameters from the background stratification. First, we converted the moored temperature data to density using a linear equation of state determined from local conductivity estimates. We then determined the background density field by low pass filtering the moored density estimates using a three-day 2nd-order Butterworth filter. For each day, we fitted a parametric double hyperbolic tangent to the background density field (a good descriptor of the density structure over the entire depth) to estimate the n-th mode structure functions, ϕ_n, and linear wave speeds, c_n. We then calculated the non-linear steepening coefficient, α_n (see Rayson et al., 2019, for a description of the relevant KdV equations and the parametric background density fit). We removed estimates of c_n and α_n when the density fit had large error.

2.3.2 Estimating wave amplitudes and bore activity

We estimated the internal wave amplitudes for the first two modes using modal amplitude fitting on the instantaneous vertical density profile obtained from 20-second thermistor data. The technique amounts to least-squares fitting the density profile to the modal structure functions to obtain a series of orthogonal isotherm excursions (Rayson et al., 2019).

We bandpass filtered the isotherm excursions to separate the M_2 internal tides from higher frequency internal waves. We then performed a Hilbert transform to obtain the mode-n internal tide amplitudes, A_{n-M2}. For the mode-1 wave field, we used a maximal overlap discrete wavelet transform (MODWT) multi-resolution analysis (MRA) to divide the super-M_2 frequencies into low- and high-frequency components, yet remove all turbulent scales (Percival & Walden, 2000). The low-frequency (LF) component contains timescales from $(2N)^{-1}$ to 4 hours, and the high-frequency (HF) component contains timescales from N^{-1} to $(2N)^{-1}$, where N is the local buoyancy frequency. We note that using a MODWT MRA differs from a conventional bandpass filter as the bounds of the effective passbands here were a function of time, allowing for local N to change as the density field was strained aperiodically over the record. For the mode-1 waves, we performed Hilbert transforms to obtain the low- and high-frequency amplitude components denoted A_{1-LF} and A_{1-HF}, respectively. Hereafter, we refer to these waves as low- and high-frequency mode-1 internal waves. For the mode-2 waves, we performed a bandpass filter between 15 minutes and 4 hours on the isotherm excursions and then performed a Hilbert transform to obtain A_2. A noteworthy limitation of WNL for this analysis is that the theory assumes that the internal wave amplitude was small with respect to the total water depth, which may result in errors in the shallower moorings where wave steepening can result in locally large internal wave amplitudes.

We followed Walter et al. (2012) and defined internal bores as sharp changes in temperature at the near-bed thermistors. We depth-averaged the thermistors in the bottom 20m and obtained the near-bed temperature anomaly θ' with a 20-minute high-pass filter, and then performed a Hilbert transform to envelop the wavetrains. This temperature anomaly θ' could potentially include other processes, such as mode-1 waves of elevation propagating near the bed or large amplitude waves of depression, which can rapidly change the near-bed temperature. Unlike Walter et al. (2012), this definition did not require both the onset and relaxation of a bore and thus included the leading/trailing edge of lower frequency processes (i.e., internal tides) that rapidly change the bottom temperature (e.g., Winters, 2015). Except for the MODWT MRA, all filtering was done with a forward-backward 2nd-order Butterworth filter using cascading second-order sections.

2.3.3 Identifying Internal Waves

After examining the records, we defined internal wave events by using specified thresholds on both wave amplitudes and the near-bed (bottom 20m) temperature anomaly, thus partitioning the observed internal waves into 5 dominant groups. In particular, events were defined to occur when $A_{1-LF} > 7.5$m, $A_2 > 7.5$m, $A_{1-HF} > 1.5$m and $\theta' > 0.6°$C. We also identified periods with hydraulic jumps by inspecting the velocity field for near-bed supercritical flows. We prevented double-counting from simultaneous wave types by only including one wave type at any moment. We counted periods with hydraulic jumps first, then internal bores, followed by whichever wave type had the largest amplitude and exceeded the relevant threshold. We also considered a 15-minute window around the exceeded threshold to include mixing on both the leading and trailing faces of the wave. We excluded concave mode-2 internal waves as internal bores often generated significant positive near-bed isotherm excursions, which contaminated the calculation of A_2.

2.4 Estimating Turbulent Diffusivities

We estimated turbulent diffusivities using independent methods based on both microstructure and finestructure measurements.

2.4.1 Microstructure Analysis

We estimated the diapycnal diffusivity K_θ using the Osborn and Cox (1972) model derived from the temperature variance equation. The model assumes a balance between the production of variance from a background vertical temperature gradient and the dissipation of variance from thermal diffusion at small scales, yielding an expression for the vertical eddy diffusivity for heat given by:

$$K_\theta = \frac{\chi}{2(\frac{d\bar{\theta}}{dz})^2} \tag{1}$$

where χ is the dissipation of thermal variance and $\frac{d\bar{\theta}}{dz}$ is the background vertical temperature gradient. Here χ was determined by first using the inertial-dissipation method (IDM) to determine the dissipation of turbulent kinetic energy ϵ (Bluteau et al., 2011). We then fitted to the inertial-convective subrange of the temperature gradient spectrum (weakly dependent on ϵ) to determine χ (Bluteau et al., 2017). For flow over the sensors of order 0.5 m/s, note that direct estimates of χ by integrating the temperature spectrum at high wavenumbers can only be used if $\epsilon < 5{\times}10^{-8} m^2 s^{-3}$ (see Bluteau et al., 2017). The IDM method has the advantage of being robust in the highly energetic flows seen at the site.

The velocity time series from the MTP was first motion corrected using the method described in Kilcher et al. (2017) and the IMU accelerometer was high-pass filtered with a 0.05 Hz 4th-order Bessel filter. The velocity record was de-spiked using the method outlined by Goring and Nikora (2002), and we removed estimates with a beam correlation lower than 80%. We split the velocity and temperature measurements into ~ 2.1 minute segments (2048 samples) overlapping by 75% for spectral fitting. We chose a segment length relatively short with respect to the typical buoyancy period (6-20 mins), and a 75% overlap to maximize the number of estimates during periods affected by NLIW, at the cost of reduced resolution at low wavenumbers and a reduced number of IDM fits at low ϵ. We rotated each segment in the velocity record such that the average segment streamwise velocity was $\bar{u}$ and the orthogonal components $\bar{v} = \bar{w} = 0$. We tested the velocity time series for each segment for stationarity and discarded segments where Taylor's frozen turbulence hypothesis was invalid ($u'_{rms}/\bar{u} > 0.15$)(Bendat & Piersol, 2010).

The spectra for both the velocity and temperature time series were calculated using Welch's method (1024 sample 50% overlapping Hanning windows). We calculated

the velocity spectra using u because of anisotropy on the transverse and vertical velocity components for low ϵ. Velocity and temperature spectra were transformed from the temporal to the spatial domain by invoking Taylor's hypothesis with a mean advection velocity $\bar{u}$. We corrected the thermistor response in the temperature spectra using a double pole transfer function (Bluteau et al., 2017) and estimates of ϵ were discarded when $Re_b = \epsilon/(\nu N^2) < 450$ (Bluteau et al., 2011).

2.4.2 Finestructure Analysis

We made an independent estimate of diapycnal diffusivity using the Prandtl mixing length model proposed by Ivey et al. (2018), which uses fine-structure (low wavenumber range of the overturning scales) turbulence observations. Ivey et al. (2018) found that:

$$K_\rho = 0.09 {L_E}^2 S \tag{2}$$

where $L_E = \tilde{\theta}/(d\bar{\theta}/dz)$ is the Ellison length scale, $\tilde{\theta}$ is the root-mean-square of the turbulent temperature fluctuations θ', $d\bar{\theta}/dz$ is the background temperature gradient and S is the background shear $d\bar{\mathbf{u}}/dz$. The model assumes that the background quantities ($d\bar{\theta}/dz$ and $d\bar{\mathbf{u}}/dz$) characterize the background environment over the vertical extent of the mixing event (in this case, L_E).

We used a MODWT to perform a scale-based decomposition of the temperature variance in order to remove contamination from the internal wave field on estimates of $\tilde{\theta}$ (N. L. Jones et al., 2020; Cimatoribus et al., 2014). The technique amounts to estimating a local minimum buoyancy period T_{Nmin} in a 60-minute window around each temperature estimate. T_{Nmin} was calculated by applying a 10-minute low-pass filter to the temperature data and converting it to density, assuming a constant salinity. We obtained $\tilde{\theta}$ by integrating the time-frequency temperature variance decomposition from the Nyquist frequency to T_{Nmin}. We then averaged the temperature variance estimates onto a 1 minute time step to match the velocity data. We estimated $\tilde{\theta}$ from both the 1 Hz and 0.05 Hz temperature data to determine the sensitivity of the variance estimates to any unresolved high frequencies.

We low-pass filtered the temperature and velocity records using a 4th-order Butterworth filter to exclude time scales shorter than T_{Nmin}. We smoothed the velocity data from the ADCPs by fitting Chebyshev polynomials and calculated the vertical shear of the horizontal velocity at the height of each thermistor. We calculated the vertical temperature gradient using 2nd-order accurate central differencing, with 1st-order accuracy at the edges.

The MODWT wavelet coefficients are variance preserving for signals with stationary backward differences, and thus we rejected any estimate of $\tilde{\theta}$ when the temperature signal had non-stationary backward differences on a window with length T_{Nmin} centered on the estimate (i.e., the largest timescale included in the temperature variance estimate). Estimates of $\tilde{\theta}$ are susceptible to underprediction due to sampling limitations and the octave passband nature of the MODWT. Depending on how the value of N_{min} compared to the wavelet coefficient frequency passbands, we sometimes excluded the contribution of the largest turbulent overturns to $\tilde{\theta}$ (to the upper limit of excluding $N_{min}/2$ to N_{min}). Similarly, we excluded contributions to $\tilde{\theta}$ from scales smaller than the Nyquist frequency. Finally, we also rejected estimates of K_ρ from equation 2 due to limitations in instrument resolution: specifically, whenever $d\bar{\theta}/dz$, $\tilde{\theta}$ and S were below $0.002°\mathrm{Cm}^{-1}$, 0.002°C and 0.004 s^{-1} , respectively.

3 Results

Using the methods described in Section 2.3, we begin with an overview of the dynamics at the site and, in particular, a description of the diverse internal wave clima-

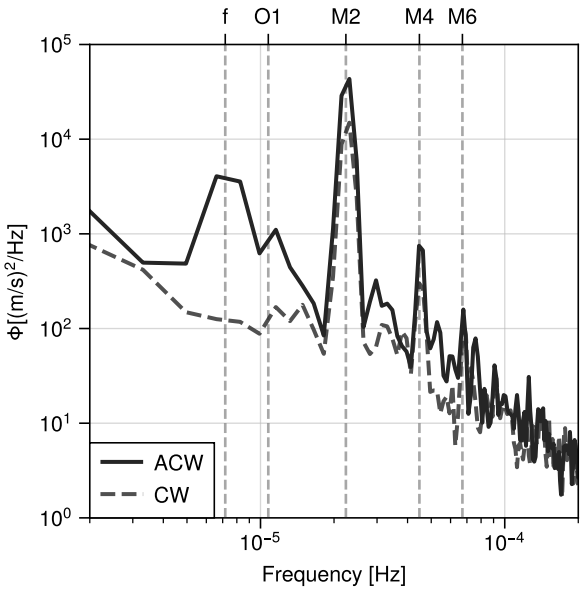

Figure 2. Rotary velocity power spectral density (PSD) from 40m depth at the 150m isobath (Welch's method, 50% overlapping ∼9 day segments). The solid and dashed lines show the anticlockwise and clockwise PSD components. Vertical dashed lines show f, O1, M2 and the first two harmonics at M4 and M6.

tology observed during the deployment. We then provide an overview of the mixing observations and the vertical turbulent heat flux driven by the forcing. Following this, we present examples of specific internal wave events and their associated mixing. Finally, we discuss the cross-shelf variability of internal wave contributions to mixing.

3.1 Site and Internal Wave Field Characterization

The barotropic velocity was dominated by the semidiurnal tide (M2) at all sites, but there were also energy peaks at the local Coriolis frequency (f), the diurnal frequency, and at the first and second harmonics of the semidiurnal tide (Figure 2). The observed anticlockwise polarized kinetic energy near f is consistent with the presence of near-inertial waves in the southern hemisphere (Alford et al., 2016). Spectral peaks at the first and second harmonic of the M_2 suggest that the tidal forcing across the ridge generated internal lee waves in the region (Rayson et al., 2018).

The spring-neap barotropic velocity amplitude varied from $\sim 0.1 - 0.3$ ms^{-1}, $\sim 0.15 - 0.5$ ms^{-1} and $\sim 0.2 - 0.7$ ms^{-1} at the 330m, 200m and 150m isobaths, respectively (Figure 3). The major axis of the tidal ellipse was approximately perpendicular to the ridge/shelf (145°) for all of the moorings, and the amplitude of the barotropic velocity increased at the shallower moorings.

From 20-24 March 2019, Severe Tropical Cyclone Veronica (hereafter, TC Veronica) passed nearby the study site, increasing the depth of the surface mixed layer, after which we observed a double pycnocline structure at the 330m and 200m depth sites until the end of the study. The depth of the lower pycnocline resulted in a strongly stratified near-bed environment at the 200m isobath. The mode-1 nonlinearity parameter, α_1, changed sign from negative (waves of depression) to positive (waves of elevation) at every mooring due to the changing stratification caused by TC Veronica (Figure 3c). There

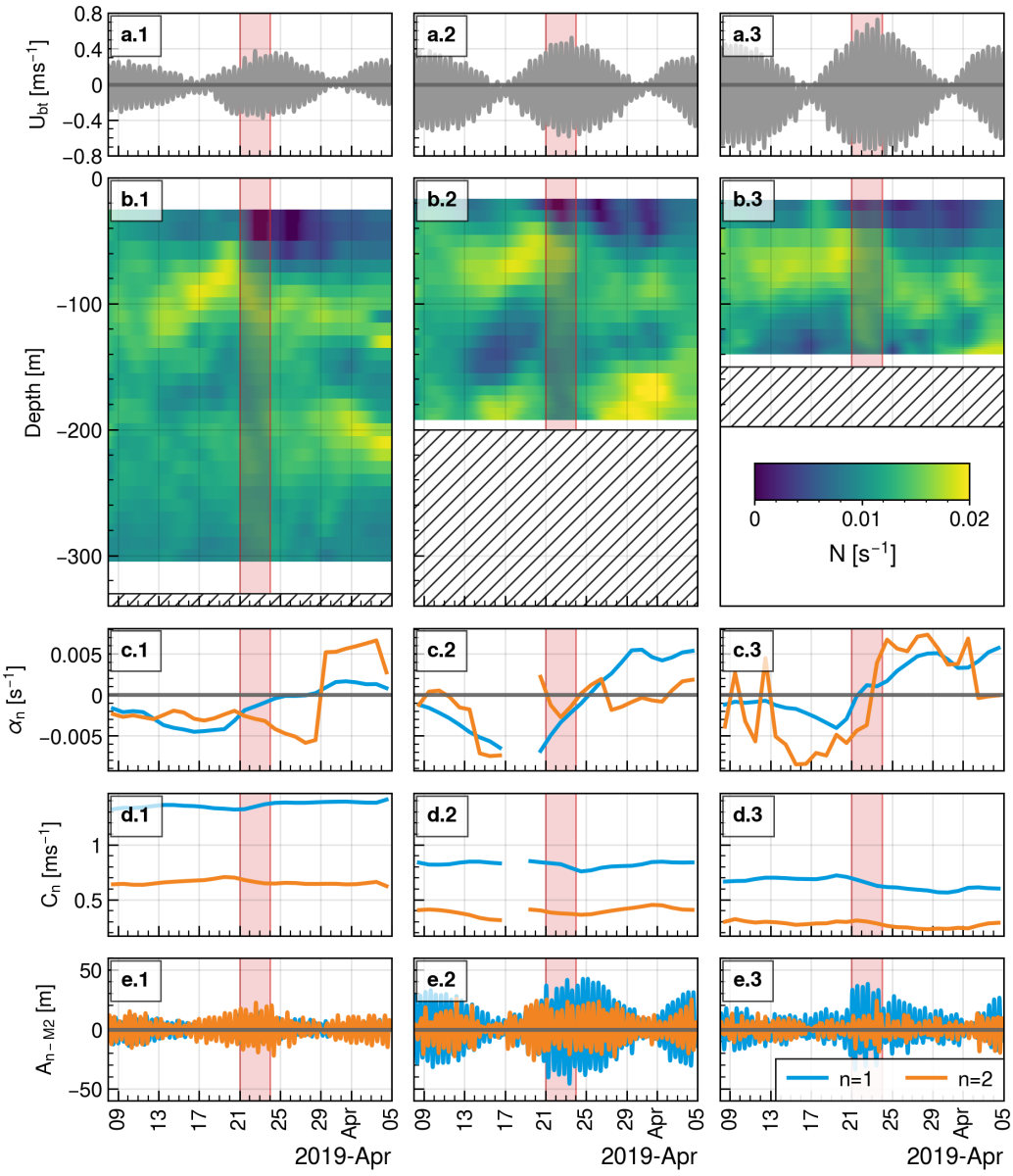

Figure 3. Columns 1-3 show observations for the 330m, 200m and 150m isobaths, respectively. Panels a.1-3, show the barotropic cross-shelf velocity from 1 min ADCP data, whilst b.1-3 show the 3-day low-pass stratification. The mode-n nonlinearity parameters, α_n, and linear wave speeds, c_n, are shown in panels c.1-3 and d.1-3, respectively. The mode-n semidiurnal internal tide amplitude A_{n-M2} is shown in panels e.1-3. Blue and orange lines represent modes 1 and 2, respectively. The pink-shaded period shows the dates when TC Veronica passed the study site.

were also rapid changes in the sign of α_2 as the maxima and minima of the mode-2 structure-function, ϕ_2, reversed.

The ratio of the semidiurnal barotropic velocity to the linear internal wave speed determines the internal Froude number $Fr_n = U_{BT}/c_n$ for each mode n. When $Fr_n > 1$, and depending on the phase, the barotropic tide was sufficiently strong to even reverse the direction of propagation of the shoaling linear waves. During this experiment, the barotropic tide was sufficiently strong to arrest linear mode-1 waves at the 150m isobath and arrest linear mode-2 waves at the 150m and 200m isobaths during the spring tides. The internal and barotropic tides showed a strong spring-neap variability. Whilst mode-1 and mode-2 M2 internal tidal amplitudes were comparable at the 330m isobath, mode-1 internal tides dominated at the shallower moorings. The mode-1 internal tide decreased in amplitude between the 200m and 150m isobaths, possibly due to a combination of energy transfer to higher frequencies and loss of energy to dissipative processes as the water depth decreased or due to destructive interference caused by wave interactions.

3.1.1 Overview of internal wave events

We identified the occurrence of five dominant types of high-frequency internal waves (periods shorter than 4 hours) using the techniques and thresholds defined in Section 2.3.3 (Figure 4). We defined the occurrence of a wave type as the percentage of time it was present with respect to the total record length. Identified internal wave events accounted for 5%, 26%, and 26% of the 28-day record at the 330m, 200m, and 150m isobaths, respectively (Figure 4e.1-3). The increased wave event occurrence at the shallower moorings was likely the result of lower frequency waves (periods longer than 4 hours) dominating at the deeper site. These lower-frequency waves were not included in our identification scheme but transferred energy to higher-frequency phenomena as they moved up the shelf and hence were identified in shallower water.

Low-frequency mode-1 internal waves were observed more frequently and with larger amplitudes as they shoaled into shallower water. The polarity of the mode-1 waves shifted from waves of depression to waves of elevation after TC Veronica changed the vertical density profile, consistent with the sign of the α_1 estimates presented in Section 3.1. These waves of elevation after TC Veronica were likely lee waves generated by the barotropic tide interacting with the nearby ridge (Legg, 2020), however, we cannot comprehensively describe lee wave generation at this site as the parameter space predicting their generation requires spatially homogeneous N and background flow which does not apply in sloping shelf seas.

Prior to TC Veronica, the observed mode-2 waves were typically confined to the thermocline and had low amplitudes. After TC Veronica formed the double pycnocline structure, convex mode-2 internal waves with larger amplitudes occurred more frequently at all three sites. From 1 April to the end of the record, we observed large amplitude mode-2 wave trains at the 330m and 200m isobaths. Oscillatory tails accompanied the mode-2 wave trains, similar to those observed on the New Jersey Shelf and in numerical/laboratory studies (Shroyer et al., 2010a; Carr et al., 2019). Feature tracking indicated that these mode-2 waves broke and transformed into waves of elevation with a high-frequency oscillatory tail, like those shown in Carr et al. (2019), before reaching the mooring at the 150m isobath.

High-frequency mode-1 internal waves occurred more frequently at the 200m and 150m isobaths, likely due to wave shoaling and breaking on the shelf. High-frequency waves occurred at the tail of other wave events, including shoaling mode-1 and mode-2 waves. Furthermore, we also observed "patches" of high-frequency waves discrete from wave events, likely the consequence of lower-frequency internal waves breaking prior to the mooring and the residual structures then being advected past the mooring by the background barotropic velocity. We also observed sustained high-frequency wave activ-

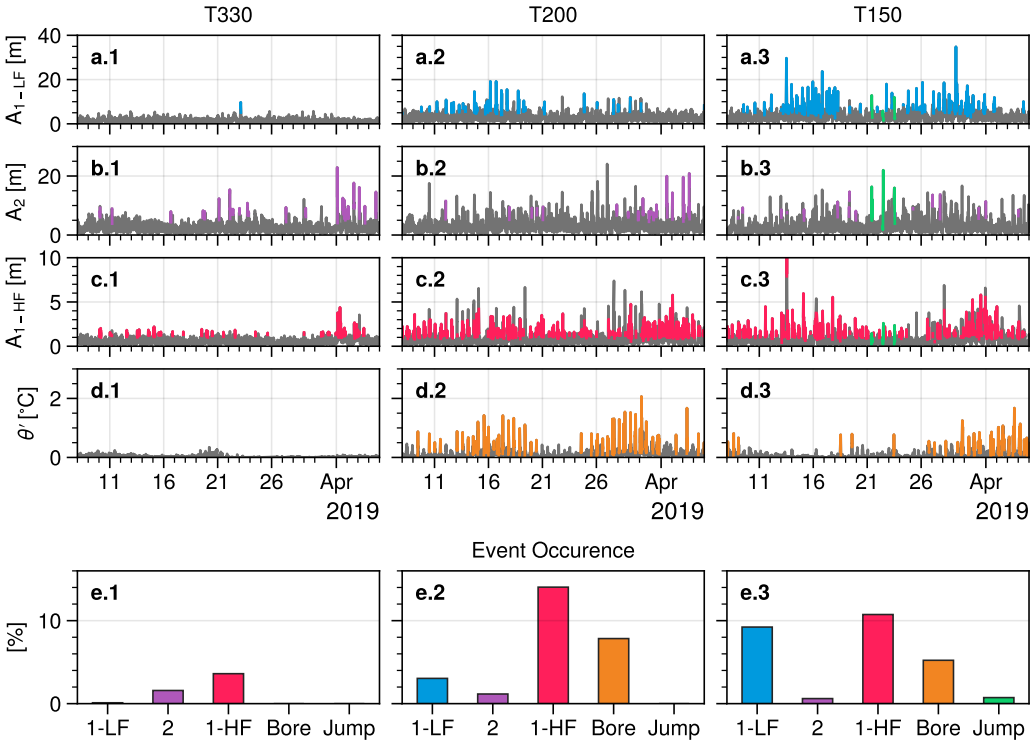

Figure 4. Columns 1, 2, and 3 represent the 330m, 200m, and 150m moorings. Rows a. to c. show the wave amplitudes for different types of internal waves. The near-bed temperature anomaly indicating bore activity is in row d. Row e shows the % occurrence of different wave events. The different types of internal wave events are shown in the same color throughout the panels. The colored lines in a-d indicate the corresponding threshold in Section 2.3.3 has been exceeded

ity in the mid-water column during and after internal bore activity at the 200m isobath, indicating the near-bed waveforms were generating a mid-water column response.

Most internal bores arrived within a few hours after the onset of the flood phase of the barotropic tide, but there was significant variation in the characteristics of the waveforms. We observed what Walter et al. (2012) termed "canonical" internal bores where, after the passage of an upwardly propagating cold front, the water column slowly returned to its initial temperature structure over several hours. The most common internal bore events, however, exhibited similar characteristics to those observed by N. L. Jones et al. (2020), where a train of trailing near-bed waves of elevation accompanied an initial cold front at the onset of the flood phase of the tide. These were distinct in character from the mode-1 waves of elevation discussed above, as isotherm excursions at the mode-1 structure function maxima were typically smaller than the near-bed excursions during these periods. We note that because these waves were sometimes large enough to be classified as LF mode-1 waves by our identification scheme, we filtered out all LF mode-1 waves that coincided with bores. Generally, tidally generated internal bores have amplitudes greater than $\delta/2$ where $\delta \approx \frac{U_0}{N}$ and U_0 is the barotropic tidal velocity amplitude (Winters, 2015). Here, δ represents the maximum vertical excursion of a particle if it converts all of its tidal kinetic energy into potential energy. Some bores had amplitudes greater than δ, indicating that there may be other internal bore generation mechanisms present.

When TC Veronica was active and near the site, low- and high-frequency mode-1, mode-2, and internal bore activity were suppressed across all sites, but we did observe three internal waves at the 150m site that exhibited the characteristics of hydraulic jumps (Nash & Moum, 2001). TC Veronica drove onshore cross-shelf (ridge) currents, which resulted in near-bed offshore return currents. The ebb flow of the barotropic tide intensified these currents, resulting in near-bed supercritical flows, which subsequently relaxed after the barotropic tides turned onshore, resulting in hydraulic jump-like features with amplitudes as large as 80m. We did not observe these waves at the deeper 200m mooring, and it was also unclear how far they moved on-shelf during the flood tide phase.

3.2 Overview of mixing estimates

3.2.1 Estimates of diffusivity

Ivey et al. (2018) demonstrated that the independent mixing estimates in equations 1 and 2 were in good agreement using data from a 100m deep site on the NWS. Our comparative microscale and finescale estimates of diffusivity, well below the main thermocline at a 200m deep site, show the same agreement over a larger range of diffusivities (Figure 5). Our diffusivity data range over nearly 6 orders of magnitude from just above $10^{-7}\mathrm{m}^2\ \mathrm{s}^{-1}$ to almost $10^{0}\mathrm{m}^2\ \mathrm{s}^{-1}$, compared to the 2.5 orders of magnitude range observed in Ivey et al. (2018). While there was scatter in individual estimates, bin-averaged estimates demonstrated excellent agreement between the two independent methods for a thermistor sampling rate f_s of 1 Hz (Figure 5a). 50% of the data were within a factor of 2, and 68% were within a factor of 4 for diffusivities above $10^{-6}\mathrm{m}^2\mathrm{s}^{-1}$, a good performance for field observations given the inherent variability in mixing model performance (Salehipour & Peltier, 2015).

We also tested the effect of decreasing the thermistor sampling frequency f_s from 1 to 0.05 Hz. The decreased sampling frequency resulted in an underestimation of the bin-averaged diffusivity by a factor of 2 at low diffusivities and 4 at high diffusivities (Figure 5b). The underestimation at lower sampling frequency resulted from a slight loss of information from high-frequency contributions to the overall temperature variance used to estimate L_E. We tested the effect of this by subsampling the FP07 thermistor data from 16Hz to 1Hz and 0.05Hz, and estimating the fraction of temperature variance resolved with respect to the total variance from 16Hz temperature data (Figure 5a-b.2). We found that almost all contributions to the temperature variance were resolved by the

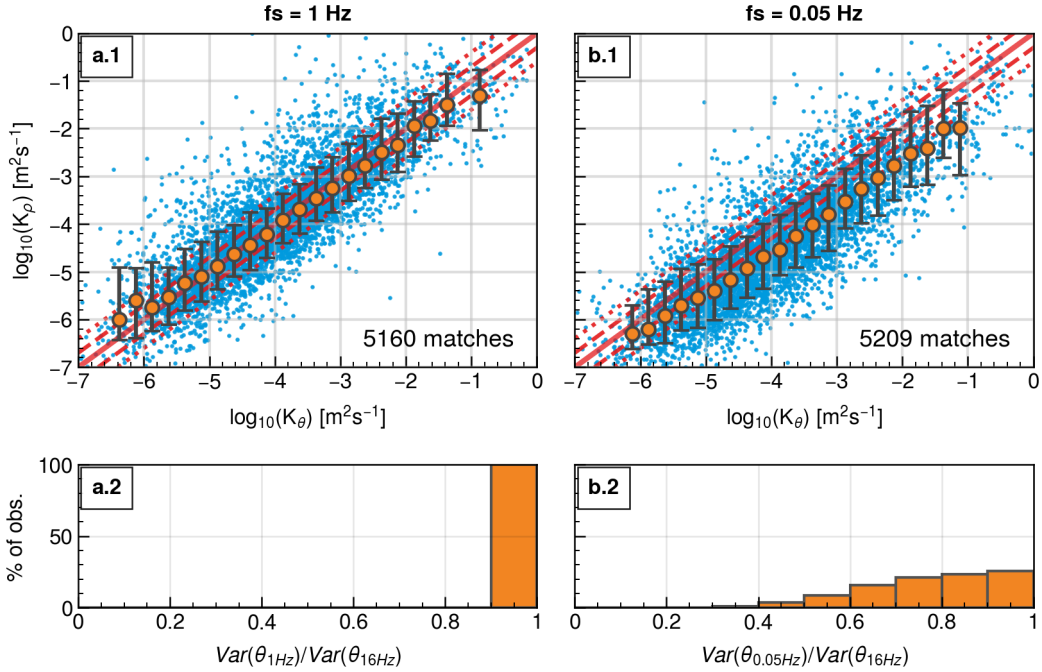

Figure 5. Comparison of diffusivity estimates K_θ and K_ρ obtained from equations 1 and 2, respectively. Columns a. and b. have thermistor sampling rates of 1 Hz and 0.05 Hz. Row 1 shows error bars spanning 0.25 decades of K_θ and describes the distribution of the matching estimates of K_ρ. Error bars are only plotted where there is a minimum of 30 matches. The orange markers and whiskers show the median and the 16th and 84th percentiles, respectively. The solid red line indicates parity between the models, and the dashed (dotted) lines indicate under-/over-estimation by a factor of 2(4). Row 2 shows histograms of the fraction of resolved temperature variance at sampling rates of 1Hz and 0.05Hz with respect to the temperature variance estimated from 16Hz data.

1Hz data, but by subsampling the temperature data to 0.05Hz we underestimated the temperature variance by a factor as large as 2. We note, however, that the degree to which the 0.05Hz data underestimated diffusivity remained relatively constant across more than five orders of magnitude. This suggests that while the higher frequency sampling was optimal, the lower-frequency thermistor data was suitable for generating comparative estimates of mixing and provides a conservative estimate of the actual diffusivity.

In the results below, we present estimates of ocean mixing derived from the fine-structure method described in Section 2.4.2, with all thermistors distributed over the water column subsampled at a common sampling frequency of $f_s = 0.05$Hz. This enables us to directly compare entire through-water-column mixing estimates for all three moorings and consequently allows us to characterize the spatiotemporal variability of mixing across the shelf.

3.2.2 Estimates of heat flux

The internal wave field caused considerable straining of the density field, so rather than examining diffusivity, we followed the approach of Shroyer et al. (2010b) and N. L. Jones et al. (2020) and quantified ocean mixing by using the vertical turbulent heat flux, $J_Q = \bar{\rho} C_p K_\rho (d\bar{\theta}/dz)$, where $\bar{\rho}$ is the average density, C_p is the heat capacity of water, and K_ρ

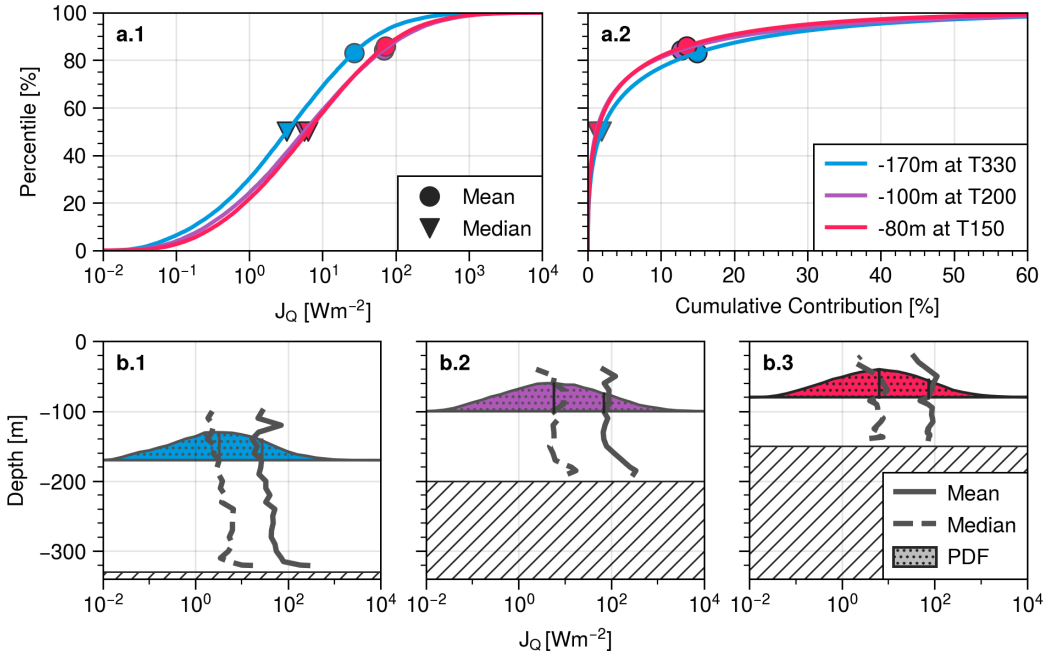

Figure 6. Summary of J_Q at the three moorings. Panels a.1 and a.2 show the distribution of J_Q and the cumulative contribution of each percentile to the net J_Q for the mid-depth thermistor at each mooring. Panels b.1-3 show the mean and median J_Q as functions of depth for each of the moorings. The colored shaded patches show examples of the probability density functions (PDF) of J_Q for the mid-depth at each mooring.

is estimated from equation 2. J_Q has the advantage of a weaker dependence on the density (temperature) gradient ($J_Q \propto (d\bar{\theta}/dz)^{-1}$, while $K_\rho \propto (d\bar{\theta}/dz)^{-2}$). Strong internal tides and large-amplitude internal waves can strain isotherms and displace the thermocline, resulting in a highly variable stratification at any given location. In these environments, and particularly in conditions when the density gradient is near well-mixed due to background (reversible) internal wave straining, J_Q provides a more meaningful description of diapycnal mixing than K_ρ.

The observed J_Q spanned 6 orders of magnitude (Figure 6a.1), a range comparable to the range in K_ρ (Figure 5). This variability was comparable to other studies that report heat and density fluxes from field observations from both finestructure (N. L. Jones et al., 2020) and microstructure (Couchman et al., 2021) turbulence observations. We used the time mean and median of J_Q at each thermistor to characterize the net and typical mixing rates. The time mean was used as a proxy for net mixing as it accounts for the total number of estimates, which can differ between thermistors due to data quality control. By rank-ordering the estimates from smallest to largest, performing the cumulative sum on the series, and then dividing each estimate by the total vertical turbulent heat flux for the entire record, we calculated the percent cumulative contribution to the turbulent heat flux for the mid-depth thermistor at each mooring (Figure 6a.2).

These cumulative contributions show that a relatively small number of energetic mixing events dominated the net heat flux during the study. Values of J_Q that exceeded the record mean accounted for 85-95% of the total vertical heat flux for all three moorings (e.g., Figure 6a.2). We, therefore, defined significant mixing events as those where the local estimate of J_Q exceeded the entire record mean. Calculating this for all ther-

mistors at all moorings thus allowed us to account for the spatial variability in the dominant events both over the depth and across the shelf (Figure 6b.1-3).

The mixing changed both with depth and across the shelf (Figure 6b.1-3). The two shallower moorings had greater mixing than the 330m mooring. Mixing at the 150m and 200m moorings was comparable, although mixing was strongest in the bottom 50m at the 200m mooring. In general, there was more variability of J_Q at the 200m mooring (e.g., the kurtosis of the PDF in Figure 6b.2) than at the other two moorings.

3.3 Characterizing internal wave driven mixing

To describe the connection between the internal wave forcing and the induced mixing, we consider 4 specific examples which characterize the type of events seen for the entire record.

3.3.1 Example 1: Shoaling mode-1 waves of depression

This example shows two mode-1 waves of depression traveling from the 200m to the 150m mooring (Figure 7). These waves marginally contributed to the net or record-long mixing at both sites, as indicated by the average heat flux during the wave exceeding the record average discussed above, especially near the surface and in the thermocline. However, both waves showed significant quiescent regions, with the average mixing beneath the wave comparable to the record median. At the 200m mooring, we observed enhanced mixing on the waves' steep leading and trailing faces, likely with contributions from local convective instabilities. Conversely, at the 150m mooring, we observed enhanced mixing only on the rear face of the wave and in the thermocline after the wave had passed, similar in form to observations reported by Moum et al. (2003), Moum et al. (2007) and Shroyer et al. (2010b) at other sites. However, J_Q observations on the trailing edge of the waves were an order of magnitude lower at our site ($\sim 10^3 \mathrm{W/m^2}$) than those observed by Shroyer et al. (2010b) ($\sim 10^4 \mathrm{W/m^2}$). We observed significant mixing beneath the wave due to shear instability associated with the baroclinic velocity. This mixing persisted for the duration of the two waves but was limited to a relatively narrow range of depths.

3.3.2 Example 2: Shoaling and breaking mode-2 waves

This example shows a convex mode-2 internal wavetrain traveling up the ridge from the 330m to 200m moorings (Figure 8). The amplitude and period of the leading mode-2 wave remained relatively constant ($\sim$15m and 15 minutes, respectively). However, by the time the waves reached the 200m mooring, the trailing waves had begun to lose coherence and resembled a trailing high-frequency mode-1 tail. The formation of a mode-1 tail behind a shoaling mode-2 wave was also observed in the field by Shroyer et al. (2010a) and laboratory/numerical studies by Carr et al. (2019).

At the 330m mooring, we observed enhanced mixing at the steep isopycnal surfaces on both the leading and trailing edges of the waves and beneath the wave trough, where the shear was large. Mixing in the wave's core was relatively quiescent, except for a thin mixing layer (< 10m) after the passage of the first wave. Outside the wave's core, the mode-2 wavetrain generated significant mixing across much of the resolved water column. By the time the wave reached the 200m mooring, we observed significant mixing ($\mathrm{J}_Q \sim 10^3 \mathrm{W/m^2}$) confined to the rear face of the wave and the high-frequency trailing waves, whilst the leading edge did not contribute substantially to mixing. The heat fluxes from the high-frequency trailing waves were comparable to those generated by the shoaling mode-2 waves at this depth.

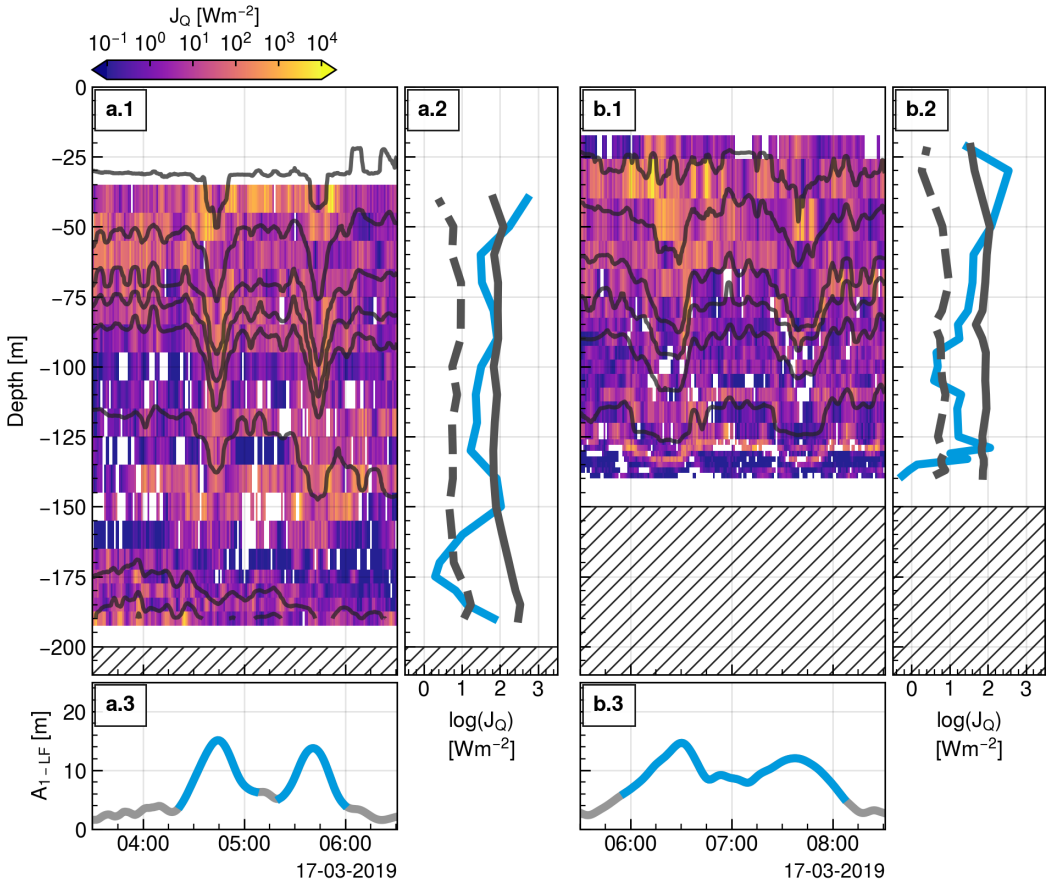

Figure 7. Panels a.1-3 and b.1-3 show a mode-1 wave of depression shoaling at the 200m and 150m isobath, respectively. The colormaps in panels a.1 and b.1 show the instantaneous vertical turbulent heat flux J_Q, with black contours showing isotherms calculated from 20-second temperature data, with a 1.5°C interval between isotherms. Panels a.2 and b.2 show the mean (solid gray) and median (dashed gray) of J_Q at each depth for the entire time series. The blue lines in panels a.2 and b.2 show the mean of J_Q for the times shown in blue in panels a.3 and b.3. Panels a.3 and b.3 show the low frequency mode-1 wave amplitudes A_1 (solid light gray), and blue lines indicate times with identified mode-1 waves.

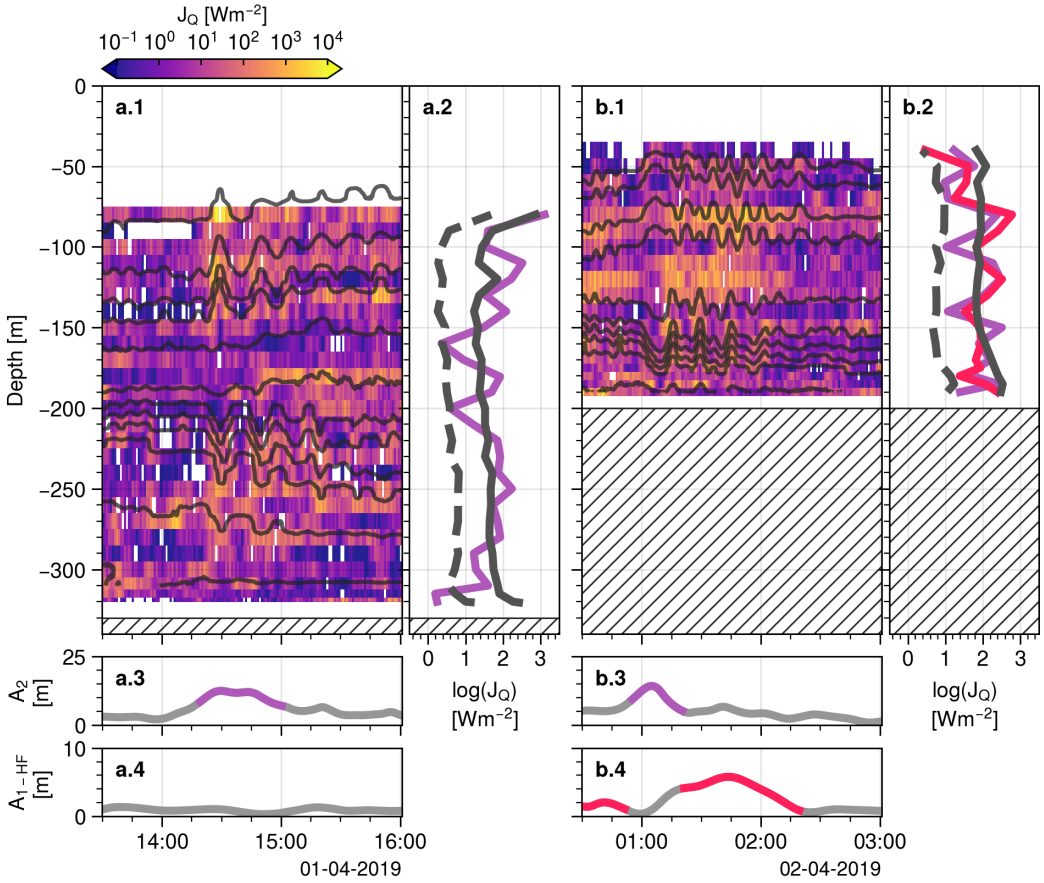

Figure 8. Same as Fig.7 but shows a convex mode-2 internal wave shoaling at the 330m and 200m mooring, respectively. The purple lines in panels a.2 and b.2 show the mean for the times shown in purple in panels a.3 and b.3. The red lines in panel b.2 shows the mean for the times shown in red in panel b.4. Panels a.3-4 and b.3-4 show A_2 and A_{1-HF} (light gray) with identified internal wave events (color) at each site, respectively.

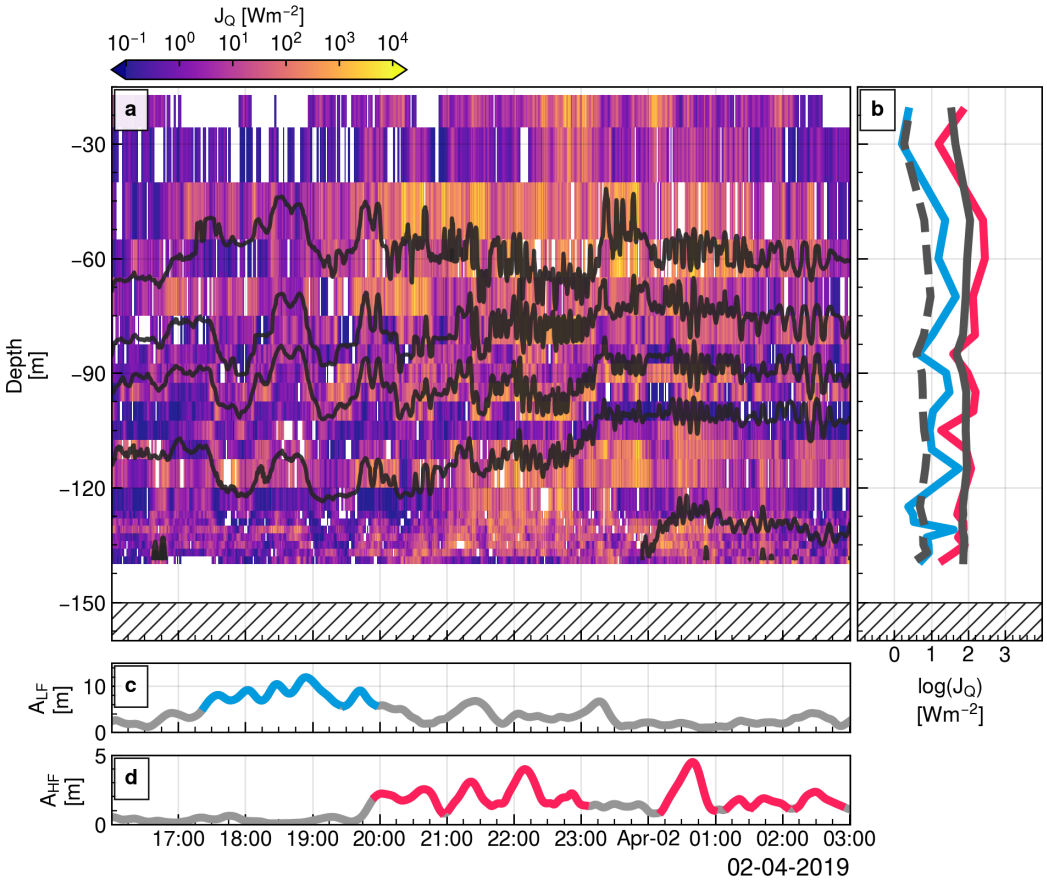

Figure 9. Wave breaking and high-frequency overturning in the lee of three mode-1 waves of elevation at the 150m mooring, likely the result of mode-2 wave breaking. In panel b, blue and red lines correspond to the time-mean J_Q for low- and high-frequency mode-1 waves, respectively. Panels c and d show A_{1-LF} and A_{1-HF},respectively. Colors indicate times with identified internal wave events. Otherwise as for Fig.7.b.

At some point between the 200m and 150m moorings, the mode-2 waves transformed into waves of elevation via a process analogous to the fission of shoaling mode-1 waves of depression (Figure 9). These mode-1 waves of elevation were an insignificant contribution to the net local mixing, with an average J_Q comparable to the record median over much of the water column. However, trailing these waves of elevation was a period with sustained high-frequency mode-1 wave activity. We observed sustained energetic mixing over much of the water column during these high-frequency waves, with instantaneous heat fluxes as large as $10^3 \mathrm{W/m^2}$. Furthermore, the average heat flux during the high-frequency trailing waves was comparable to the record average over much of the depth, indicating sustained significant mixing.

3.3.3 Example 3: Internal Bores

Internal bores contributed significantly to near-bed mixing. In this example, a train of 12 internal bores moved up the ridge at the 200m mooring at the start of the flood phase of the barotropic tide (Figure 10). The amplitude of the waves was ∼25m, with periods slightly longer than the local buoyancy period (∼6 minutes). The bores were not

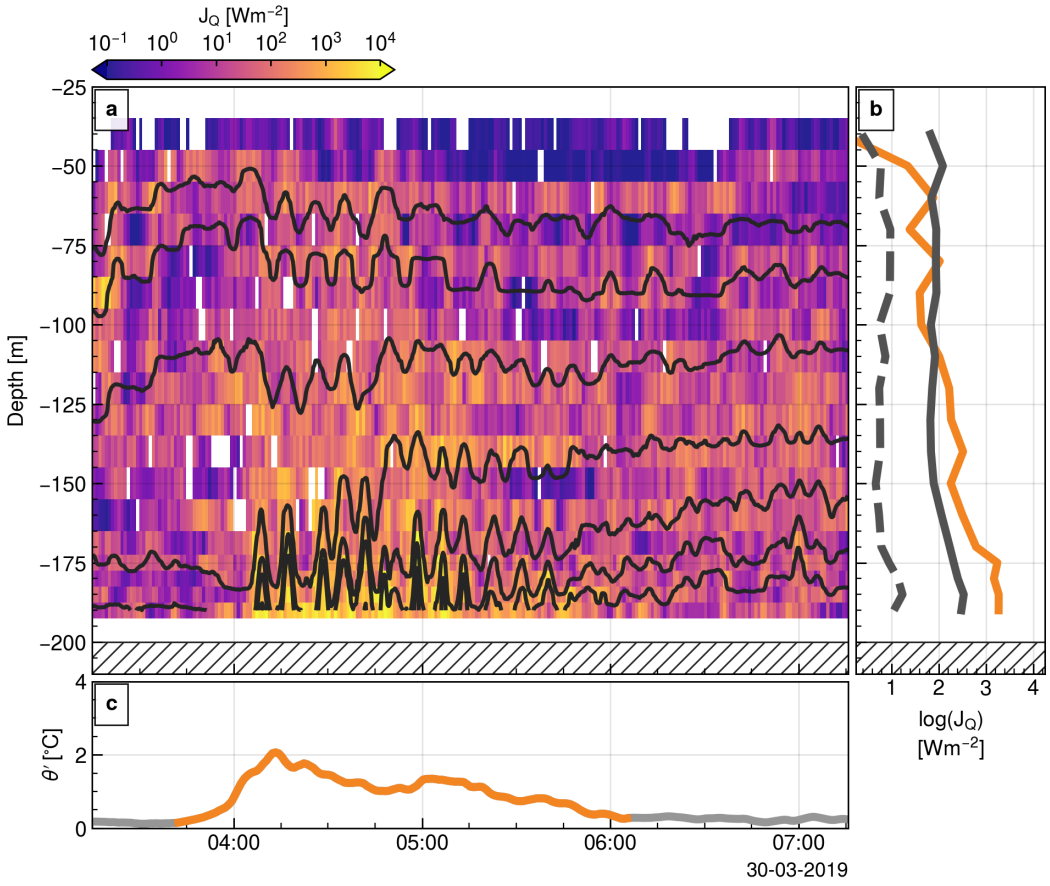

Figure 10. An internal bore at the 200m mooring. The orange line in panel b shows the arithmetic average of J_Q for the times shown in orange in panel c. Panel c shows the near-bed high-frequency temperature anomaly. Otherwise, identical to Fig.9.

observed at the deepest mooring and thus were generated between the 330m and 200m moorings. During this period, the internal bore amplitudes were much larger than $\delta = U_0/N \approx 10$m, indicating that the bore did not form directly from the barotropic tide (i.e., Winters, 2015). Furthermore, the bores did not form due to the polarity reversal of α_1 as there was no turning point between the 330m and 200m moorings. The bores also affected the dynamics higher in the water column, as evidenced by ∼10m amplitude in-phase internal waves at the thermocline.

The internal bore train greatly enhanced mixing near the bed, with heat fluxes as large as 10^4W/m^2 sustained for the first six waves in the packet. Winters (2015) observed that tidally generated internal bores could enhance mixing over a height of up to 5δ above the bed. However, the bore in this example was much stronger and significantly enhanced mixing over 10δ (100m) above the bed. The average mixing decayed away from the bed, with an average heat flux comparable to the record mean at the surface. Heat flux estimates within the wave train were comparable to those observed in N. L. Jones et al. (2020), where they observed fluxes as large as 10^4W/m^2. Both the leading and trailing faces of the waves show significant mixing, likely via the different breaking processes described in N. L. Jones et al. (2020). We note that both the temporal and spatial sampling (1 minute and ∼5m, respectively) was relatively large compared to the period and amplitude of the observed waves (6 minutes and ∼25m).

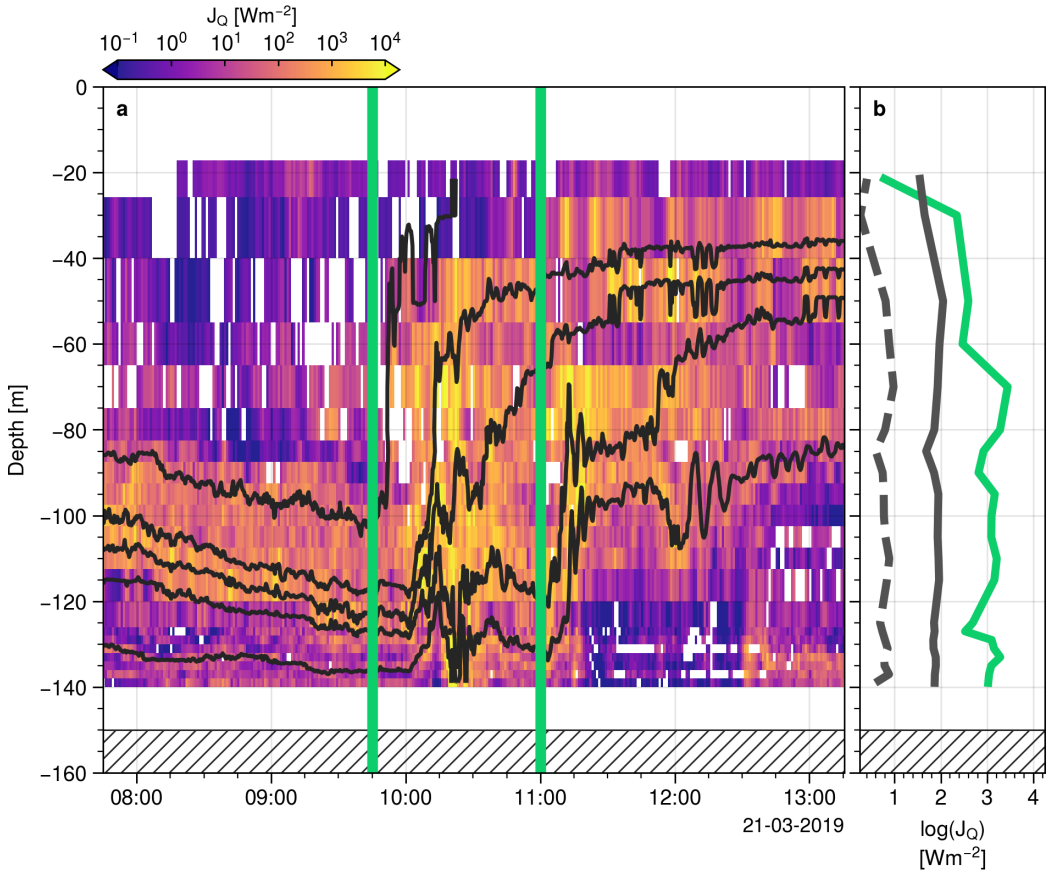

Figure 11. A hydraulic jump observed at the 150m isobath. The green line in panel b shows the mean of J_Q for the times bounded by the green vertical lines in panel a. Solid and dashed lines show the mean and median vertical heat flux at the 150m isobath for the entire record. Otherwise identical to Fig.10a

3.3.4 Example 4: Hydraulic Jump

Hydraulic jumps exhibited some of the most intense mixing in the entire record. We selected the first of three hydraulic jumps observed at the 150m mooring during TC Veronica as an example. (Before the onset of the hydraulic jump, we observed $\mathrm{Ri} = \mathrm{N}^2/\mathrm{S}^2 < 0.25$ (not shown) at the thermocline due to the wind-driven onshore currents above the thermocline and energetic near-bed offshore currents. This period showed sustained significant mixing ($\mathrm{J}_Q \sim O(10^3 - 10^4)\mathrm{W/m}^2$) across the thermocline due to shear-driven instabilities. At the onset of the flood phase of the barotropic tide, we observed a jump of scale ~70m. The jump generated intense overturning, resulting in heat fluxes as large as $10^4\mathrm{W/m}^2$ over much of the water column. The average heat fluxes were consistently 1-2 orders of magnitude greater than the record median, similar to the observations by Nash and Moum (2001). Furthermore, the average heat fluxes greatly exceeded the record average in depths greater than 125 m (~40% of the water depth).

3.4 The Cross-Shelf Evolution of NLIW-driven Mixing

Using the wave identification schemes from Section 2.3.3 and the mixing estimates from Section 2.4.2, we determined the vertical heat flux associated with the dominant

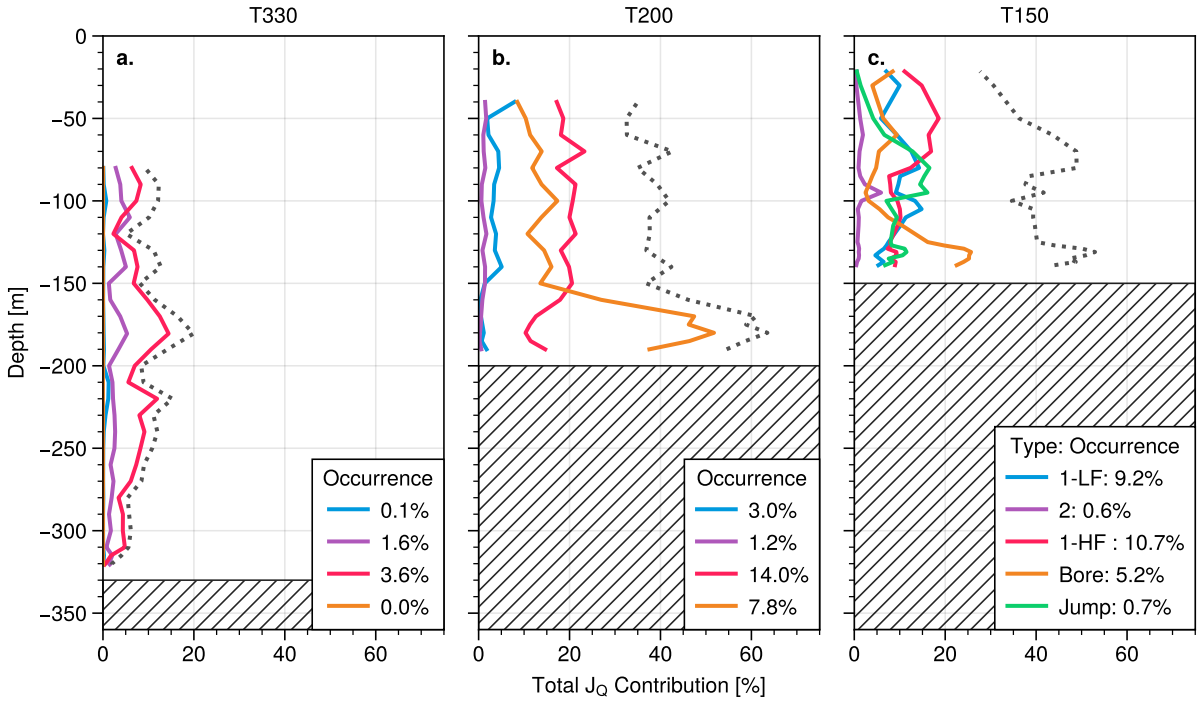

Figure 12. The total vertical heat flux contribution (%) of the different internal wave types at the 330m, 200m and 150m moorings, respectively. The wave occurrence is shown in the legends for each plot. Dotted lines show the sum of all contributions at each site. The hatched regions show the depth at each location.

internal wave types (defined in Section 2.3.3) at each site (Fig. 12). This allowed us to account for both the frequency of internal waves and their mixing magnitude when determining which internal wave processes were the most important for mixing on the shelf. We remind the reader that the identification schemes exclude internal waves with periods longer than 4 hours and amplitudes lower than the relevant thresholds.

The identified internal waves accounted for a significant portion of the total vertical heat flux, especially at the shallower moorings. The identified internal waves at the 200m and 150m moorings occurred relatively frequently (∼26% occurrence) and accounted for up to 60% and 50% of the total observed heat flux, respectively. Despite these categories of internal waves being relatively rare at the 330m mooring (5% occurrence), they accounted for as much as 20% of the vertical heat flux, indicating that the identified internal waves remained an important mixing source despite occurring less frequently.

The increased internal wave contribution to the total heat flux at the shallower sites was consistent with increasing non-linearity and breaking as the waves shoal. However, the fact that the observed internal wave-driven mixing was greater at the 200m mooring than at the 150m mooring indicates that factors other than simply the depth (i.e., stratification, slope) were also affecting the location of internal wave-driven mixing hot spots.

We assessed the variability of the direct internal wave-driven mixing, defined as when waves and mixing are temporally co-located across the shelf and over the depth. This analysis only accounts for the direct mixing of each wave type and does not include the indirect mixing that may occur after a wave transfers its energy to other processes. For

example, in the case shown in Section 3.3.2, the energetic mixing during the high-frequency mode-1 waves was only attributed to high-frequency mode-1 waves despite forming as a result of mode-2 wave breaking.

The internal wave processes driving mixing changed substantially in the 26km between the 330m and 200m moorings and again in the 6km between the 200m and 150m moorings. High-frequency mode-1 waves were generally the most significant contributors to mixing at each site, likely due to their formation during wave breaking. However, internal bores dominated mixing near the sea bed at the shallower sites and remained a significant mixing source through the water column at the 200m mooring. Given α did not change polarity between the 330m and 200m mooring, it was unclear exactly where these bores were generated and over what distance they contributed to elevated mixing.

At the 330m and 200m moorings, low-frequency mode-1 and mode-2 waves were relatively unimportant to the total vertical heat flux. Low-frequency mode-1 waves contributed comparably to high-frequency waves and bores at the 150m site. Despite occurring infrequently, hydraulic jumps contributed comparably to the other internal waves at the 150m mooring. However, due to the mooring positions, the horizontal spatial extent of the mixing remained unclear.

4 Conclusions

The fine-structure mixing model proposed by Ivey et al. (2018), with temperature variance estimates from time-frequency decomposition (i.e. N. L. Jones et al., 2020), provided good estimates of diffusivity over a wide range of flows when compared to the microstructure diffusivity estimates at the same site. These fine-structure mixing estimates provided estimates of the vertical turbulent heat flux over much of the water column over the 30-day deployment. We found that rare energetic mixing events dominated the total vertical heat flux across the entire deployment for each depth/mooring. This suggests that rather than reproducing the typical (median) mixing, capturing the intermittent but energetic mixing events is required to accurately represent mixing processes in coastal ocean models. This also implies that the assumption of a constant mixing efficiency, an assumption which is not supported for high vertical turbulent density fluxes (Couchman et al., 2021), may result in poor estimates of the vertical heat fluxes in these environments.

We observed the spatial and temporal distributions of mixing for multiple internal wave types to determine how significant these waves were for mixing and how this changed across the shelf. The mean and median heat fluxes at the 330m mooring were smaller than at the two shallower sites. The shallower sites showed comparable heat fluxes, except near the bed at the 200m mooring due to the localized presence of internal bores (Fig. 6). The spatiotemporal distribution of mixing was highly dependent on the wave type and depth. Generally, low-frequency mode-1 and mode-2 waves created small, transient regions of enhanced mixing as they traveled up the slope but did not generate sufficient sustained energetic mixing to dominate the total mixing, especially at the deeper sites. Instead, these low-frequency waves transferred energy to high-frequency processes that, in turn, greatly enhanced mixing. This suggests that rather than estimating the mixing generated from propagating non-breaking internal waves, it is critical to determine the location and duration of internal wave breaking events and their associated mixing within ocean models.

Quantifying internal wave breaking is particularly challenging in ocean circulation models as there are inadequate representations of non-linear internal wave processes in these models (Luneva et al., 2019; Vlasenko et al., 2014). Internal wave breaking observed at this site indicates that convective instabilities (N. L. Jones et al., 2020; Chang et al., 2021) are important in driving diapycnal mixing. Even simple parameterizations of mix-

ing based on the Richardson number (i.e., Ivey et al., 2021; Large et al., 1994) require modeling the combined effects of both baroclinic and barotropic processes. Thus, the artificial prevention of non-linear wave steepening intended to prevent models from becoming unstable inhibits the development of convective instabilities in non-hydrostatic ocean circulation models. Furthermore, baroclinic energy on the NWS is typically remotely generated (Rayson et al., 2011; Gong et al., 2021), indicating that mixing parameterizations based solely on the local barotropic-baroclinic conversion (i.e., Inall et al., 2021) would not account for the breaking internal waves observed at this site. More complicated two-equation closure schemes commonly used in circulation models also fail to accurately represent mixing in shelf seas (Luneva et al., 2019; Savelyev et al., 2022).

Internal bores significantly contributed to the near-bed heat flux and enhanced mixing throughout much of the water column. These bores were generated between the 330m and 200m moorings and showed signs of dissipating by the 150m mooring, indicating that these waves may contribute to mixing over a distance between 10-40km for this site. Similarly, internal hydraulic jumps generated turbulent flows and large mixing estimates, despite their infrequent occurrence. We did not observe these jumps at the 200m mooring, indicating that they did not contribute to mixing more than 6km offshore from the 150m mooring. However, barotropic tides may have swept the jumps and any remnant mixing activity onshore of the ridge. Furthermore, it was unclear if the occurrence of the hydraulic jumps was representative of longer timescales or if the jumps only occurred due to the wind stress imposed by TC Veronica. The existing parameter spaces for both lee waves/hydraulic jumps (Legg, 2020) and tidally generated internal bores (Winters, 2015) do not account for vertically variable stratification or horizontally variable tidal velocity amplitudes, making them difficult to apply on continental shelves where both quantities are highly variable.

We found that a set of relatively simple wave amplitude/temperature anomaly thresholds resolved a significant portion of the mixing, especially in the shallower moorings. The dominant internal wave types for mixing varied significantly as a function of depth across the shelf. However, determining what processes are associated with the unattributed mixing remains an important task for process-based parameterizations of mixing on continental shelves. Areas for future study include quantifying the mixing contributions of low-frequency processes (e.g., shear generated by the internal tide induced baroclinic velocities) and processes smaller (in amplitude) than the arbitrary thresholds defined in this work. Furthermore, it is unclear how to best account for the mixing contributions of different concurrent internal wave processes, which confounds the attribution of mixing to different wave types, resulting in uncertainty when evaluating process-based mixing parameterizations. Nonetheless, the findings of this research have significant implications for determining which internal wave processes are the most important to parameterize and what vertical and horizontal grid scales are required to adequately resolve the spatial variability of ocean mixing.

5 Data Availability Statement

The temperature, velocity, and microstructure data used in for this analysis are available on the University of Western Australia's research repository (https://doi.org/10.26182/7r84-e088). Examples of the computational notebooks used to reproduce this analysis can be found on Zenodo (https://doi.org/10.5281/zenodo.7587748).

Acknowledgments
The authors thank Andrew Zulberti, Amy Waterhouse and Ian Milne for their practical and technical advice during this analysis. We also thank the AIMS staff and the R.V. Solander crew for their assistance during the fieldwork. This work was funded by an Australian Research Council (ARC) Research Training Program Scholarship, a Samaha Re-

search Top-Up Scholarship, the ARC Industrial Transformation Research Hub for Offshore Floating Facilities (IH140100012), and ARC Discovery Project "Quantifying and parameterizing ocean mixing" (DP180101736).

References

Aghsaee, P., Boegman, L., & Lamb, K. G. (2010). Breaking of shoaling internal solitary waves. *Journal of Fluid Mechanics*, *659*, 289–317. doi: 10.1017/S002211201000248X

Alford, M. H., Mackinnon, J. A., Simmons, H. L., & Nash, J. D. (2016). Near-Inertial Internal Gravity Waves in the Ocean. *Annual Review of Marine Science*, *8*, 95–123. doi: 10.1146/annurev-marine-010814-015746

Bendat, J. S., & Piersol, A. G. (2010). *Random Data*. Hoboken, NJ, USA: John Wiley & Sons, Inc. doi: 10.1002/9781118032428

Bluteau, C. E., Jones, N. L., & Ivey, G. N. (2011). Estimating turbulent kinetic energy dissipation using the inertial subrange method in environmental flows. *Limnology and Oceanography: Methods*, *9*(JULY), 302–321. doi: 10.4319/lom.2011.9.302

Bluteau, C. E., Lueck, R. G., Ivey, G. N., Jones, N. L., Book, J. W., & Rice, A. E. (2017). Determining mixing rates from concurrent temperature and velocity measurements. *Journal of Atmospheric and Oceanic Technology*, *34*(10), 2283–2293. doi: 10.1175/JTECH-D-16-0250.1

Carr, M., Stastna, M., Davies, P. A., & van de Wal, K. J. (2019). Shoaling mode-2 internal solitary-like waves. *Journal of Fluid Mechanics*, *879*, 604–632. doi: 10.1017/jfm.2019.671

Chang, M. H., Lien, R. C., Lamb, K. G., & Diamessis, P. J. (2021). Long-Term Observations of Shoaling Internal Solitary Waves in the Northern South China Sea. *Journal of Geophysical Research: Oceans*, *126*(10). doi: 10.1029/2020JC017129

Cimatoribus, A. A., Van Haren, H., & Gostiaux, L. (2014). Comparison of ellison and thorpe scales from Eulerian ocean temperature observations. *Journal of Geophysical Research: Oceans*, *119*(10), 7047–7065. doi: 10.1002/2014JC010132

Couchman, M. M., Wynne-Cattanach, B., Alford, M. H., Caulfield, C. c. P., Kerswell, R. R., MacKinnon, J. A., & Voet, G. (2021). Data-Driven Identification of Turbulent Oceanic Mixing From Observational Microstructure Data. *Geophysical Research Letters*, *48*(23), e2021GL094978. doi: 10.1029/2021GL094978

Davis, K. A., Arthur, R. S., Reid, E. C., Rogers, J. S., Fringer, O. B., DeCarlo, T. M., & Cohen, A. L. (2020). Fate of Internal Waves on a Shallow Shelf. *Journal of Geophysical Research: Oceans*, *125*(5), e2019JC015377. doi: 10.1029/2019JC015377

Ghassemi, A., Zahedi, S., & Boegman, L. (2022). Bolus formation from fission of nonlinear internal waves over a mild slope. *Journal of Fluid Mechanics*, *932*. doi: 10.1017/JFM.2021.1033

Gong, Y., Rayson, M. D., Jones, N. L., & Ivey, G. N. (2019). The effects of remote internal tides on continental slope internal tide generation. *Journal of Physical Oceanography*, *49*(6), 1651–1668. doi: 10.1175/JPO-D-18-0180.1

Gong, Y., Rayson, M. D., Jones, N. L., & Ivey, G. N. (2021). Directional decomposition of internal tides propagating from multiple generation sites. *Ocean Modelling*, *162*, 101801. doi: 10.1016/J.OCEMOD.2021.101801

Goring, D. G., & Nikora, V. I. (2002). Despiking Acoustic Doppler Velocimeter Data. *Journal of Hydraulic Engineering*, *128*(1), 117–126. doi: 10.1061/(ASCE)0733-9429(2002)128:1(117)

Huisman, J., Pham Thi, N. N., Karl, D. M., & Sommeijer, B. (2006). Reduced mix-

ing generates oscillations and chaos in the oceanic deep chlorophyll maximum. *Nature*, *439*(7074), 322–325. doi: 10.1038/nature04245

Inall, M. E., Toberman, M., Polton, J. A., Palmer, M. R., Green, J. A., & Rippeth, T. P. (2021). Shelf Seas Baroclinic Energy Loss: Pycnocline Mixing and Bottom Boundary Layer Dissipation. *Journal of Geophysical Research: Oceans*, *126*(8). doi: 10.1029/2020JC016528

Ivey, G. N., Bluteau, C. E., Gayen, B., Jones, N. L., & Sohail, T. (2021). Roles of Shear and Convection in Driving Mixing in the Ocean. *Geophysical Research Letters*, *48*(3). doi: 10.1029/2020GL089455

Ivey, G. N., Bluteau, C. E., & Jones, N. L. (2018). Quantifying Diapycnal Mixing in an Energetic Ocean. *Journal of Geophysical Research: Oceans*, *123*(1), 346–357. doi: 10.1002/2017JC013242

Jones, H. A. (1970). *The sediments, structure, and morphology of the northwest Australian continental shelf between Rowley Shoals and Monte Bello Islands. Record 1970/027* (Tech. Rep.). Canberra: Geoscience Australia.

Jones, N. L., Ivey, G. N., Rayson, M. D., & Kelly, S. M. (2020). Mixing Driven by Breaking Nonlinear Internal Waves. *Geophysical Research Letters*, *47*(19). doi: 10.1029/2020GL089591

Kilcher, L. F., Thomson, J., Harding, S., & Nylund, S. (2017). Turbulence measurements from compliant moorings. Part II: Motion correction. *Journal of Atmospheric and Oceanic Technology*, *34*(6), 1249–1266. doi: 10.1175/JTECH-D-16-0213.1

Lamb, K. G. (2014). Internal wave breaking and dissipation mechanisms on the continental slope/shelf. *Annual Review of Fluid Mechanics*, *46*, 231–254. doi: 10.1146/annurev-fluid-011212-140701

Large, W. G., McWilliams, J. C., & Doney, S. C. (1994). Oceanic vertical mixing: A review and a model with a nonlocal boundary layer parameterization. *Reviews of Geophysics*, *32*(4), 363–403. doi: 10.1029/94RG01872

Legg, S. (2020). Mixing by Oceanic Lee Waves. *Annual Review of Fluid Mechanics Annu. Rev. Fluid Mech. 2021*, *53*, 173–201. doi: 10.1146/annurev-fluid-051220

Luneva, M. V., Wakelin, S., Holt, J. T., Inall, M. E., Kozlov, I. E., Palmer, M. R., ... Polton, J. A. (2019). Challenging Vertical Turbulence Mixing Schemes in a Tidally Energetic Environment: 1. 3-D Shelf-Sea Model Assessment. *Journal of Geophysical Research: Oceans*, *124*(8), 6360–6387. doi: 10.1029/2018JC014307

MacKinnon, J. A., & Gregg, M. C. (2003). Mixing on the Late-Summer New England Shelf—Solibores, Shear, and Stratification. *Journal of Physical Oceanography*, *33*(7), 1476–1492. doi: 10.1175/1520-0485(2003)033⟨1476:MOTLNE⟩2.0.CO;2

Moum, J. N., Farmer, D. M., Shroyer, E. L., Smyth, W. D., & Armi, L. (2007). Dissipative Losses in Nonlinear Internal Waves Propagating across the Continental Shelf. *Journal of Physical Oceanography*, *37*(7), 1989–1995. doi: 10.1175/JPO3091.1

Moum, J. N., Farmer, D. M., Smyth, W. D., Armi, L., & Vagle, S. (2003). Structure and Generation of Turbulence at Interfaces Strained by Internal Solitary Waves Propagating Shoreward over the Continental Shelf. *Journal of Physical Oceanography*, *33*(10), 2093–2112. doi: 10.1175/1520-0485(2003)033

Nash, J. D., & Moum, J. N. (2001). Internal hydraulic flows on the continental shelf: High drag states over a small bank. *Journal of Geophysical Research: Oceans*, *106*(C3), 4593–4611. doi: 10.1029/1999jc000183

Osborn, T. R., & Cox, C. S. (1972). Oceanic Fine Structure. *Geophysical Fluid Dynamics*, *3*, 321–345.

Percival, D. B., & Walden, A. T. (2000). *Wavelet methods for time series analysis*. Cambridge University Press.

Rayson, M. D., Ivey, G. N., Jones, N. L., & Fringer, O. B. (2018). Resolving high-frequency internal waves generated at an isolated coral atoll using an unstructured grid ocean model. *Ocean Modelling*, *122*, 67–84. doi: 10.1016/j.ocemod.2017.12.007

Rayson, M. D., Ivey, G. N., Jones, N. L., Meuleners, M. J., & Wake, G. W. (2011). Internal tide dynamics in a topographically complex region: Browse Basin, Australian North West Shelf. *Journal of Geophysical Research: Oceans*, *116*(1). doi: 10.1029/2009JC005881

Rayson, M. D., Jones, N. L., & Ivey, G. N. (2019). Observations of large-amplitude mode-2 nonlinear internal waves on the australian north west shelf. *Journal of Physical Oceanography*, *49*(1), 309–328. doi: 10.1175/JPO-D-18-0097.1

Salehipour, H., & Peltier, W. R. (2015). Diapycnal diffusivity, turbulent Prandtl number and mixing efficiency in Boussinesq stratified turbulence. *Journal of Fluid Mechanics*, *775*, 464–500. doi: 10.1017/jfm.2015.305

Savelyev, I. B., Martin, P. J., Fan, Y., Savidge, D. K., Shearman, R. K., Haack, T., ... Wang, Q. (2022). An Empirical Evaluation of Turbulence Closure Models in the Coastal Ocean. *Journal of Geophysical Research: Oceans*, *127*(4), e2021JC017588. doi: 10.1029/2021JC017588

Shroyer, E. L., Moum, J. N., & Nash, J. D. (2010a). Mode 2 waves on the continental shelf: Ephemeral components of the nonlinear internal wavefield. *Journal of Geophysical Research*, *115*(C7). doi: 10.1029/2009jc005605

Shroyer, E. L., Moum, J. N., & Nash, J. D. (2010b). Vertical heat flux and lateral mass transport in nonlinear internal waves. *Geophysical Research Letters*, *37*(8). doi: 10.1029/2010GL042715

Vlasenko, V., Stashchuk, N., Inall, M. E., & Hopkins, J. E. (2014). Tidal energy conversion in a global hot spot: On the 3-D dynamics of baroclinic tides at the Celtic Sea shelf break. *Journal of Geophysical Research: Oceans*, *119*(6), 3249–3265. doi: 10.1002/2013JC009708

Walter, R. K., Brock Woodson, C., Arthur, R. S., Fringer, O. B., & Monismith, S. G. (2012). Nearshore internal bores and turbulent mixing in southern Monterey Bay. *Journal of Geophysical Research: Oceans*, *117*(7). doi: 10.1029/2012JC008115

Waterhouse, A. F., Mackinnon, J. A., Nash, J. D., Alford, M. H., Kunze, E., Simmons, H. L., ... Lee, C. M. (2014). Global patterns of diapycnal mixing from measurements of the turbulent dissipation rate. *Journal of Physical Oceanography*, *44*(7), 1854–1872. doi: 10.1175/JPO-D-13-0104.1

Whalen, C. B., de Lavergne, C., Naveira Garabato, A. C., Klymak, J. M., MacKinnon, J. A., & Sheen, K. L. (2020). Internal wave-driven mixing: governing processes and consequences for climate. *Nature Reviews Earth and Environment*, *1*(11), 606–621. doi: 10.1038/s43017-020-0097-z

Winters, K. B. (2015). Tidally driven mixing and dissipation in the stratified boundary layer above steep submarine topography. *Geophysical Research Letters*, *42*(17), 7123–7130. doi: 10.1002/2015GL064676

Wyatt, A. S., Leichter, J. J., Toth, L. T., Miyajima, T., Aronson, R. B., & Nagata, T. (2020). Heat accumulation on coral reefs mitigated by internal waves. *Nature Geoscience*, *13*(1), 28–34. doi: 10.1038/s41561-019-0486-4